Humidity sensing potential of Fe_2TiO_5—pseudobrookite

M. V. Nikolić[1*], M. D. Luković[1], Z. Ž. Vasiljević[2], N. J. Labus2, O. S. Aleksić[1]

[1] Institute for Multidisciplinary Research, University of Belgrade, Kneza Viseslava 1, Belgrade 11000, Serbia

[2] Institute of Technical Sciences of the Serbian Academy of Sciences and Arts, Belgrade, Serbia

Abstract

Bulk samples of pseudobrookite with an orthorhombic crystal structure were prepared by sintering a mixture of starting hematite and anatase nano powders in the weight ratio 60:40 at three different sintering temperatures (950, 1050 and 1150 °C) resulting in different microstructures determined by SEM analysis. Humidity sensing properties of pseudobrookite were investigated by measuring changes in electrical properties at operating temperatures of 20, 40 and 60 °C in the frequency range 100 Hz–100 kHz in the relative humidity range 30–90% in a climatic chamber. At 100 Hz, and 20 °C the impedance of pseudobrookite sintered at 1150 °C reduced over 5 times in the humidity range 40–90%, and 7 times at 60 °C for pseudobrookite sintered at 950 °C. Detailed analysis of dielectric properties showed that the dielectric constant increased noticeably with increase in humidity at low frequencies. Electrical conductivity change with frequency followed the Jonscher power law, and increased with increase in relative humidity. The determined frequency constant reduced with increase in sample temperature and increase in relative humidity. The conduction mechanism can be explained using the correlated barrier hopping model. Analysis of complex impedance using an equivalent circuit showed the dominant influence of grain boundaries. Low hysteresis (3.6 and 2.99%) was obtained in the 40–90% humidity range at room temperature (25 °C) for pseudobrookite sintered at 950 and 1150 °C.

1 Introduction

Reliable and accurate measurement of water content in different environments and materials remains significant, as water is one of the essential components of all living organisms, the biosphere and materials on Earth [1]. Monitoring, detection and control of ambient humidity

* M. V. Nikolic, mariav@afrodita.rcub.bg.ac.rs

under varied temperature conditions (low to high temperatures) or in a mixture with other gases is essential [2]. Different working principles and diverse materials have been used in moisture/humidity sensors as an answer to demands of different operating conditions and many different areas of application ranging from indoor to open air use. The term moisture is usually used when detecting the water content in liquids and solids, while humidity is used when detecting the water vapor content in gases [1]. Humidity sensors are mainly used to determine the water content in air or other gases [1]. Relative humidity (RH) is defined as the ratio of the amount of water vapor present in the atmosphere to the maximum amount the atmosphere can hold at a same given temperature and pressure of gas [2]. It depends on temperature and is stated as a percentage [2]. It is the most convenient and commonly applied measurement method [1]. The basic requirement of a good humidity sensor is good sensitivity over a wide range of water content and tempera- ture, short response time, good reproducibility, low cost and maintenance, small hysteresis, long life, easy fabrication, small size/weight, compatibility with microprocessor etc [1]. In their comprehensive review, Faharani et al. [2] categorized humidity sensors according to their fabrication technologies, sensing materials, working and operating principles. Many different materials that include ceramic, polymer and composite materials and their combinations (organic/ inorganic hybrid sensors) have been used as humidity sensing materials [2]. Ceramic humidity sensors have been and remain in focus as they have good thermal and environmental stability, good response and mechanical strength, wide range of operating temperatures, low fabrication cost and robustness. They are most often made using metal oxides such as SnO_2, ZnO, TiO_2, Fe_2O_3 and WO_3 [1, 3], often spinel [4–6] or perovskite type oxides [7–9] and their compositions [10–12]. Dopants are often applied to enhance metal oxide properties for gas sensing [12–16]. The humidity sensing mechanism of metal oxides is simple and is based on water adsorption on the ceramic surface [1]. The structure of these materials consisting of grains, grain boundaries and pores directly influences and utilizes changes in the physical and electrical properties of sensitive elements when exposed to different atmospheric humidity conditions and different gases [1].The functionality of metal oxides is linked with the degree of non-stoichiometry and the presence of structural defects [1]. The effects of dopants was noted in changes in the charge/ionic volume ratio and the concentration on the surface leading to increase in the number of adsorption sites for water molecules [17].

Ceramic humidity sensors can be fabricated as a sintered pellet (bulk), thick or thin film [3]. Bulk or sandwich type humidity sensors are the oldest and simplest type. However, as the main processes in gas and humidity sensors take place on the surface or in a near-surface thin layer,

the maximum response is lower in bulk than for thin or thick film sensors [3]. Thin and thick film sensors are usually fabricated by depositing a sensing layer over electrodes printed on an insulating substrate [3]. Work on improvement of ceramic humidity sensors can be in improving the material or the design. In improving the material, research can focus on developing a new material or improving the properties of an existing one (such as nanostructuring or doping) [1].

Pseudobrookite is a semiconducting metal oxide with an n-type narrow band gap of ~ 2.2 eV similar to hematite (α-Fe_2O_3) [18]. As its valence band edge surpasses water oxidation and its conduction band minimum is near the energy level of TiO_2 it has recently been investigated as a potential material for visible-light water oxidation [18]. Pseudobrookite with an orthorhombic crystal structure can be obtained through the solid state reaction of anatase (TiO_2) and hematite (Fe_2O_3) at sintering temperatures above 800 °C. In our previous work we performed a detailed analysis of the sintering temperature effect on structural and electricalproperties of pseudobrookite obtained by solid state synthesis from starting anatase and hematite nanopowders [19]. Hematite (α-Fe2O3) has been the subject of extensive research as a gas sensing material [3]. Yu et al. [20] determined that Fe2TiO5 enhanced gas sensing properties of Fe_2O_3 hollow spheres towards ethanol. The potential of pseudobrookite as a possible gas sensing material has previously been investigated towards NO [21]. In this work we focus on investigating pseudobrookite (Fe2TiO5) as a possible humidity sensing material. Taking into account that the microstructure of a metal oxide material plays a crucial role in the gas sensing mechanism, in this work we have chosen three different samples from the microstructure viewpoint and investigated in detail the influence of humidity on changes in dielectric and electric properties.

2 Experimental

2. 1 Disc fabrication

Starting hematite (Alfa Aesar, 99%, grain size 20–60 nm) and anatase (Alfa Aesar, 99.7% anatase, grain size 15 nm) nanopowders were mixed in the weight ratio 60:40 in a planetary ball mill (Fritsch Pulversisette 5) in stainless steel bowls with stainless steel balls for 60 min (ball to powder ratio 20:1). Disc shaped green samples, 10 mm in diameter and average thickness 1.23 mm, were formed using 0.25 g of the hematite-anatase nanopowder mixture, by applying pressure of 200 MPa in a RING P-14 VEB THURINGER Hydraulic press. Green samples were sintered in air at 950, 1050 and 1150 °C (denoted as S1, S2 and S3,

respectively) for two hours. Sample density was determined from weight and volume (dimension) measurements. The average green sample density was determined as 2.59 g/cm^3.

2. 2 Characterization

XRD patterns were recorded on a RIGAKU RINT2000 diffractometer, CuK_α = 1.54178 Å. SEM analysis was per- formed on a TESCAN Electron Microscope VEGA TS 5130 MM device, while EDS analysis was performed on a INCA Penta FETX3 energy dispersive system. Images were observed on freshly fractured samples. The average grain size was estimated from SEM images by averaging at least 100 grains on analyzed SEM micrographs.
Samples were prepared for electrical measurements by coating with silver paste resulting in good ohmic contacts. Silver electrodes were deposited on both sides preparing disc samples in capacitor form electrically equivalent to a capacitance C_p in parallel with resistance R_p. Admittance was calculated as:

$$Y = \frac{1}{Z} = \frac{1}{R_p} + j\omega C_p = G + jB = j\omega C_0\left(\varepsilon'_r - \varepsilon''_r\right) = \omega C_0 \varepsilon''_r + j\omega C_0 \varepsilon'_r \quad (1)$$

where C_0 is the capacitance of the corresponding air gap of a parallel plate capacitor with dimensions corresponding to the dimensions of the tested sample, ω is the angular frequency, G and B are the real and imaginary parts of admittance, enabling calculation of the real and imaginary parts of complex permittivity s^f also known as the dielectric constant and ε''_r.
The dielectric loss tangent was calculated as $tgD = \varepsilon''_r / \varepsilon''_r$, while AC conductivity was determined as: $\sigma_{AC} = \omega\varepsilon_0\varepsilon''_r$, where ε_0 is the permittivity of free space of vacuum.
Measurements were conducted in a JEIO TECH TH-KE-025 temperature and humidity climatic chamber on a JEIO TECH TH-KE-025 temperature and humidity climatic chamber on aHP4274A multifrequency LCR meter in the frequency range 100 Hz–100 kHz. Change of impedance, resistance and capacitance with change in sample temperature (0–80 °C) was initially measured. The influence of change in humidity (40–90%) on impedance, resistance and capacitance at the operating temperature of 20 °C, and 30–90% at 40 and 60 °C for S1, S2 and S3 samples was measured. Absorption and desorption curves were measured at the operating temperature of 25 °C at 100 Hz in the relative humidity range of 40–90%. Response and recovery times were also measured at the operating temperature of 25 °C at 100 Hz.

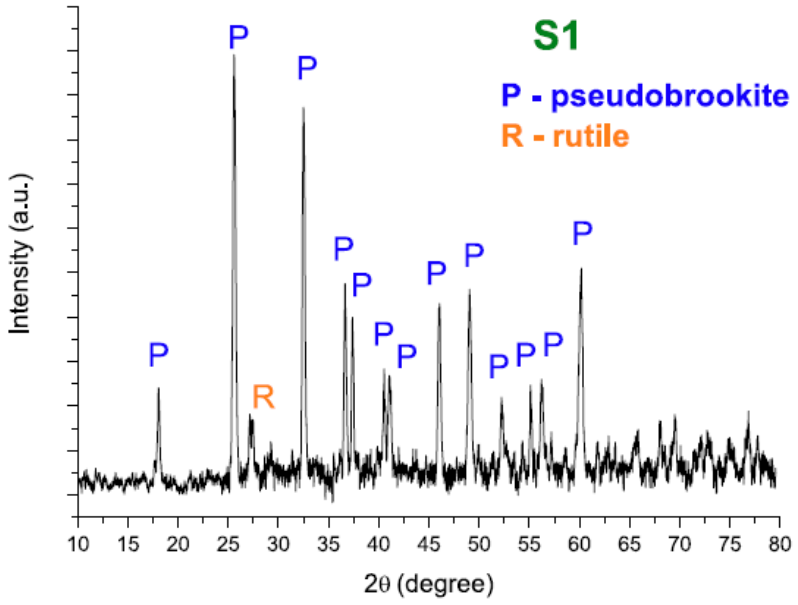

Fig. 1 XRD pattern of sample S1

3 Results and discussion

3.1 Structural analysis

XRD analysis of sintered samples, described in detail in [19] showed that samples S1–S3 were composed of pseudobrookite (orthorhombic crystal structure) and a small amount of rutile (Fig. 1). The greatest difference is in the sample density and microstructure, as shown in Fig. 2. Sample S1 (Fig. 2a, b), sintered at 950 °C has a relatively homogenous grain size distribution with an average grain size of 0.54 μm, density 3.63 g/cm^3 (83.39% ρ_T—theoretical density). Porosity is high, with noticeable open pores between grains. Just a few small closed pores within grains can be noted, as shown on Fig. 2a. Sample S2 (Fig. 2c, f) sintered at 1050 °C, density 3.86 g/cm^3 (88.67% ρ_T) exhibits an inhomogeneous microstructure consisting of noticeable large grains surrounded by many smaller grains. The influence of sintering temperature on grain growth is noticeable when we compare Fig. 2b (sintering temperature 950 °C) and 2c (sintering temperature 1050 °C) recorded with the same magnification of ×7500. Though density is higher, we can note small closed pores within the grains and also larger pores between grains. The average grain size (as described in detail in [19]) of smaller grains was 0.95 μm, while the average dimensions of the large rods was 4.13 μm length and 1.94 μm width. Sample S3 (Fig. 2d, e) sintered at 1150 °C consisted of overall larger grains as grain growth of smaller grains still noticeably continued with increase in the sintering temperature.

This is noticeable if we compare Fig. 2e (sintering temperature 1150 °C) and Fig. 2f (sintering temperature 1050 °C) recorded with the same magnification of ×3000. The average grain size was 5.27 µm, averaging both much larger and smaller grains. It was difficult to discern both rod dimensions so this is an overall average. Sample density was slightly higher at this sintering temperature achieving 3.93 g/ cm^3 (90.28% ρ_T). Pores between relatively large sintered grains are still noticeable as shown in Fig. 2d. Many more closed pores can also be noted within the large rod shaped grains, as shown in Fig. 2d, e. EDS analysis enabled identification of individual quite large rutile grains (marked in Fig. 2e as R) together with the predominant pseudobrookite grains.

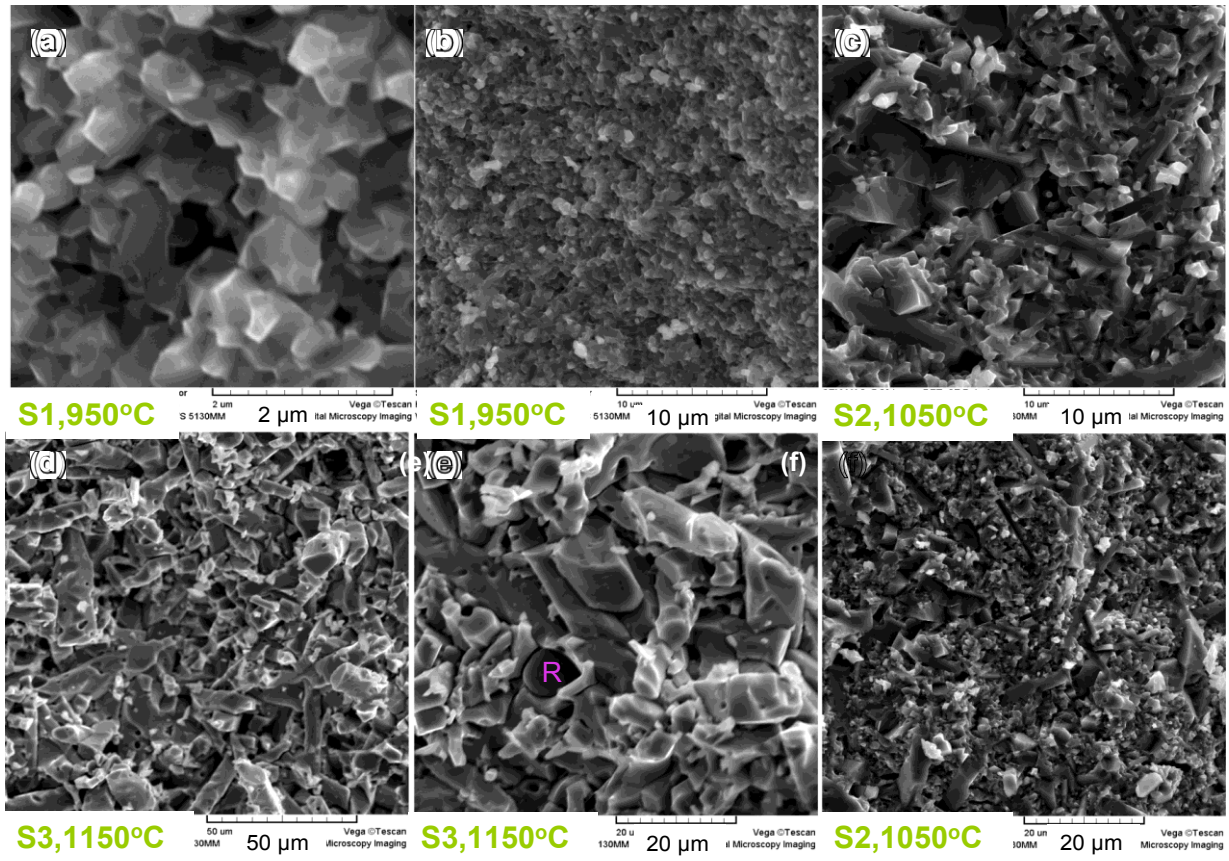

Fig. 2 SEM images of samples S1—(**a, b**); S2—(**c, f**) and S3—(**d, e**)

3.2 Temperature response

Previous investigation of electrical properties of pseudobrookite bulk samples (described in detail in [19]) showed that with increase in the sintering temperature the electrical resistivity decreased, while the dielectric constant and the electrical conductivity increased. This is in accordance with the change of measured impedance values for samples S1, S2 and S3 at 20 °C

for different frequencies shown as an inset in Fig. 3, where the highest impedance was measured for S1 and the lowest for S3 reflecting the influence of the sintering temperature on sample density and microstructure. For all three analyzed samples the measured impedance decreased with increase in applied frequency following an exponential dependence, so it was the highest for 100 Hz. Measured impedance also decreased with increase in sample temperature as shown for sample S3 in Fig. 3. The difference between measured impedance values with increase in frequency reduced.

The temperature response can be defined as the relative change in relative impedance with temperature:

$$\Delta|Z| = \left(\frac{|Z|_0 - |Z|_T}{|Z|_0}\right) \times 100\% \qquad (2)$$

where $|Z|_0$ is the initial impedance of the sensor, $|Z|_T$ is the impedance at different temperatures.

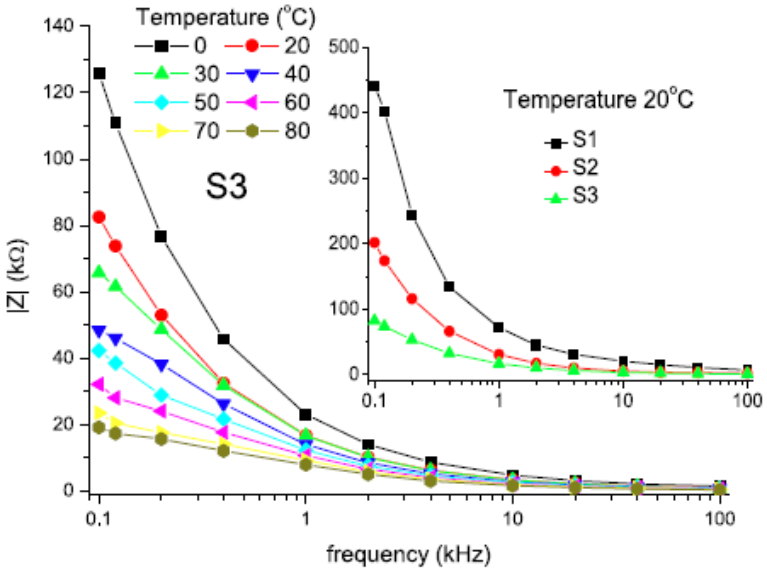

Fig. 3 Change of impedance for sample S3 with frequency at different temperatures, inset change of impedance with frequency for samples S1, S2 and S3 at 20 °C

With increase in sample temperature, the largest value was obtained for S3 of 1.57, with 1.06 for S1 and 0.97 for S2 at 100 Hz.

3.3 Humidity sensing response

To investigate the effect of frequency on the sensing characteristics of analyzed S1, S2 and S3

pseudobrookite samples measurements have been conducted with different test frequencies, ranging from 100 Hz to 100 kHz at the 3 analyzed operating temperatures of 20, 40 and 60 °C and range of humidity from 30 to 90% RH. For all three analyzed samples the measured impedance/resistance and capacitance values changed the most with increase in humidity for all three measured temperatures (20, 40 and 60 °C) for the lowest applied frequency of 100 Hz. An example is given in Fig. 4, showing the reduction of impedance with frequency (Fig. 4a) for different humidity values and change of impedance with humidity (Fig. 4b) for different applied frequencies for sample S1 measured at 40 °C. The highest impedance values and the most expressed changes were noted for the applied frequency of 100 Hz. Change of impedance, resistance and capacitance with humidity for samples S1, S2 and S3 (applied frequency 100 Hz) is shown in Fig. 5 for the three analyzed operating temperatures of 20, 40 and 60 °C. If we observe change in impedance for samples S1, S2 and S3 for the operating temperature of 20 °C, it is noticeable that the impedance changes the most with increase in humidity for sample S3. In the measured humidity range (40–90%) the impedance reduced 4.11 times for sample S3 (from 93 to 22 kΩ), while it reduced only 1.88 times for sample S1 (526–280 kΩ) and 1.55 times for sample S2 (207–133 kΩ). Similar differences were noted for increase in capacitance and decrease in resistance for samples S1, S2 and S3. In the case of samples S1 and S3 a more rapid reduction in resistance/impedance was noted for humidity in the range 70–90%. Increase in operating temperature to 40 °C resulted in an overall reduction in impedance/resistance and increase in capacitance. Increase in sample temperature did not have any noticeable influence on sample S2, where the impedance reduced 1.59 times (149.7–93.9 kΩ), and this continued for the operating temperature of 60 °C (1.6—122.6 to 73.1 kΩ for humidity 30–90%). In the case of sample S1, at 40 °C the impedance reduced 2.96 times (376.2–126.9 kΩ) for humidity ranging from 30 to 90%, with a slightly more rapid decrease in impedance starting at relative humidity of 60%. The greatest change in impedance at 40 °C was noted for sample S3 of 5.46 times (60.5–11 kΩ). Increase in operating temperature to 60 °C resulted in similar shaped impedance curves for samples S1 and S3, with impedance decreasing 6.9 times for sample S1 (208.4–30.2 kΩ) and 5.37 times for sample S3 (34.1–6.3 kΩ). Thus in the case of sample S1 which had the smallest average grain size reduction of impedance became more expressed with increase in sample operating temperature (1.88 for 20, 3 for 40 and 6.9 times for 60 °C), while for sample S3 with a larger average grain size and density the increase in operating temperature from 40 to 60 °C did not further influence the decrease in impedance with increase in sample humidity.

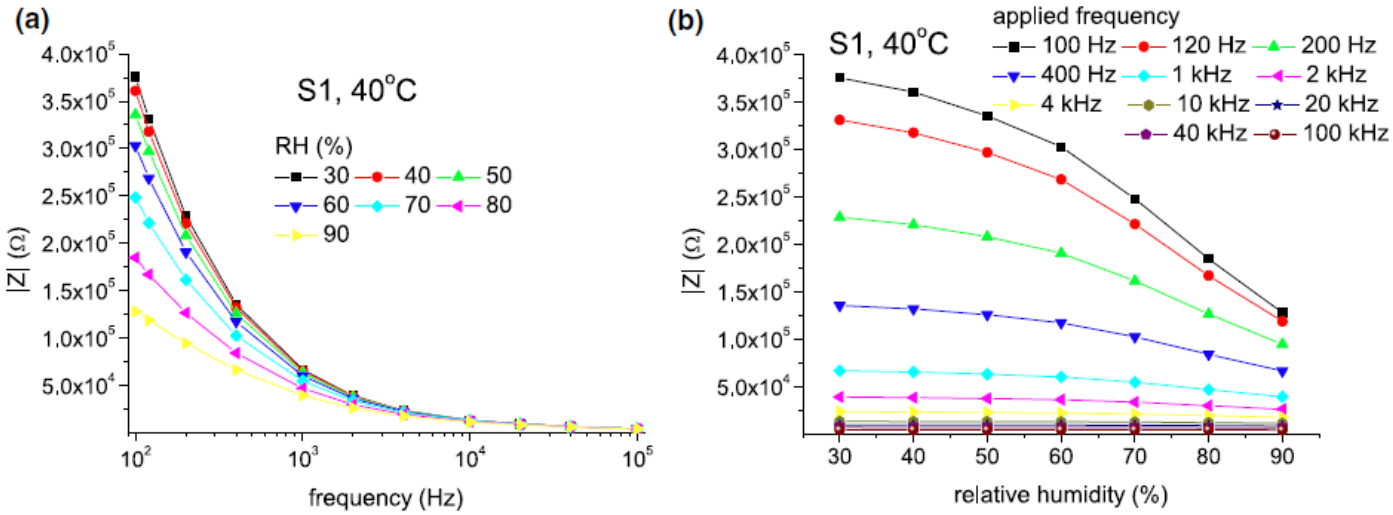

Fig. 4 Change of impedance of sample S1 at 40 °C with frequency (**a**) for different humidity values and humidity (**b**) for different applied frequencies

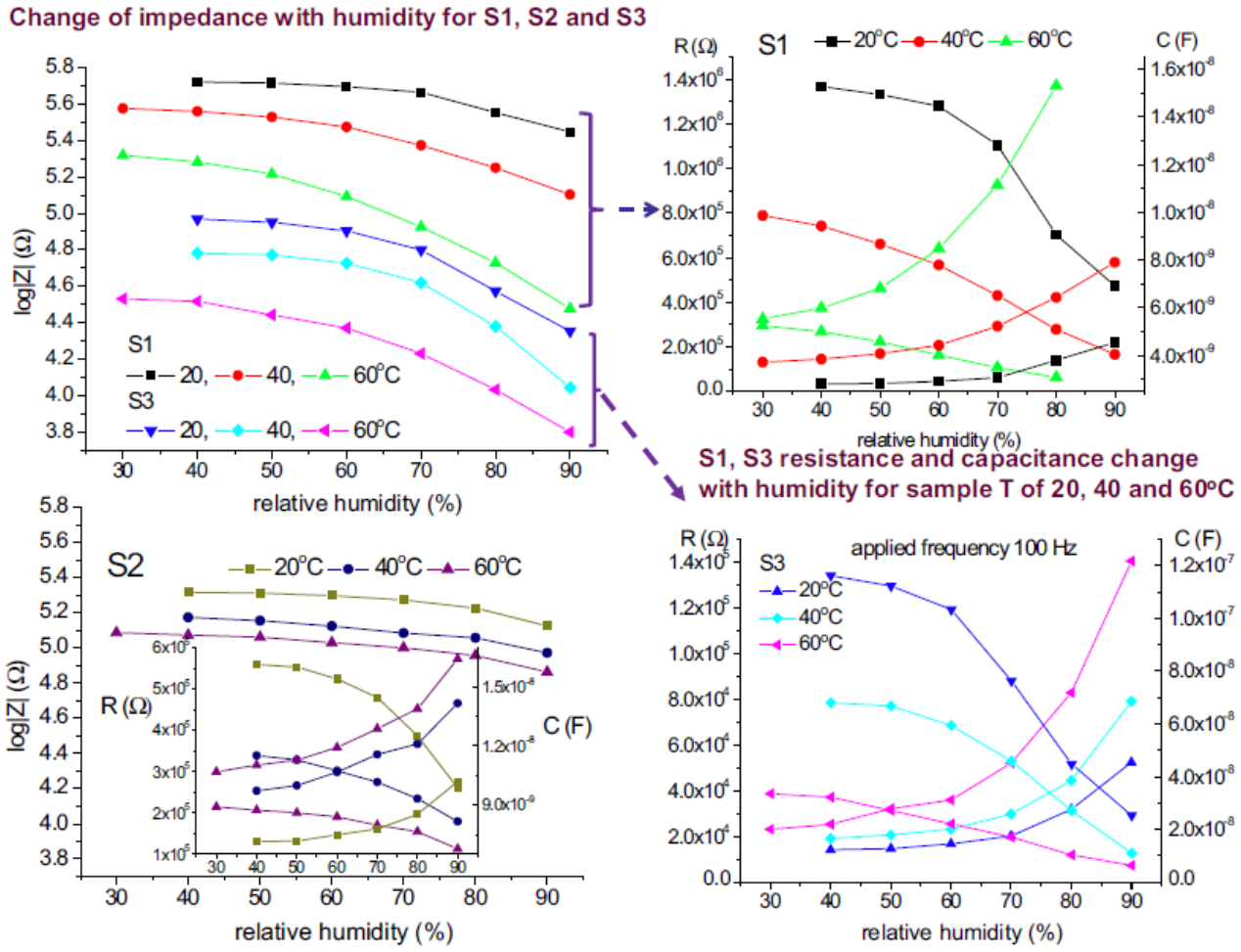

Fig. 5 Change of impedance of samples S1, S2 and S3 with humidity at applied frequency of 100 Hz

The sensitivity (sensor response) can be defined as:

$$S = \frac{|Z|_{LH} - |Z|_H}{|Z|_{LH}} \times 100, \qquad (3)$$

where $|Z|_{LH}$ is the impedance measured at the lowest analyzed humidity and $|Z|_H$ is the impedance measured for different humidity values in the chamber. The calculated sensitivity for samples S1, S2 and S3 in the measured humidity ranges (40–90% at 20 °C) and 30–80% at operating temperatures of 40 and 60 °C are shown in Fig. 6. The obtained results for sensitivity correspond with the previously analyzed change of impedance. The highest sensitivity at the operating temperature of 20 °C was obtained for sample S3. The sensitivity of sample S1 improved with increase in operating temperature and was the highest at 60 °C. These changes are closely correlated with the sample grain size, grain size distribution and porosity that have a significant influence on the resulting response to change in humidity [13]. The presence of intergranular and intragranular porosity, the determined pore size and distribution are also deter- mining factors in humidity sensing [2]. All these factors are closely linked with the humidity sensing mechanism of pseudobrookite.

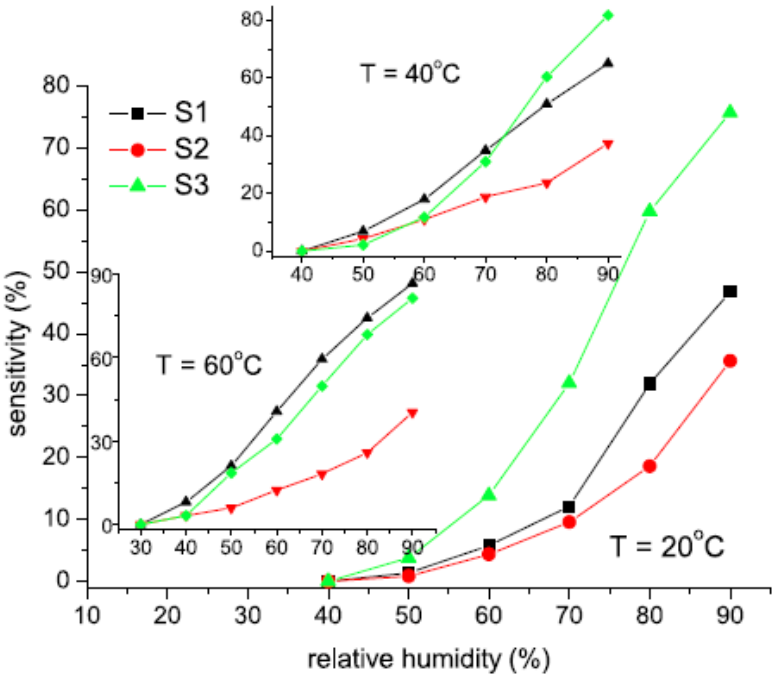

Fig. 6 Sensitivity of samples S1, S2 and S3 as a function of relative humidity

3.4 Humidity sensing mechanism

The humidity sensing mechanism of metal oxides can be explained as adsorption of water molecules on the ceramic sample surface [2, 9, 22]. It is characterized by two processes. A schematic illustration of the humidity sensing mechanism is shown in Fig. 7. When exposed to humidity active sites on the surface retain water molecules. Thus, water molecules are first chemisorbed onto available active sites. Chemisorption is a dynamic process. As relative humidity increases a chemisorbed layer is formed on the sample surface. Measured impedance values are high as significant energy is required for the hopping transfer of protons between adjacent hydroxyl groups. Adsorbed water reacts with the surface by a dissociative mechanism. Water is adsorbed with the hydrogen side on the surface and due to the high interaction energy, water dissociates to a hydroxyl firmly attached to the surface [23]. As the humidity increases water molecules are physically adsorbed on the first layer. They form a double hydrogen bond and can- not move freely. The physisorbed water easily dissociates to form hydronium ions (H_3O^+) due to high electrostatic fields in the chemisorbed layer. With further humidity increase at a certain point second or multi physisorbed layers form by physisorption of water molecules onto available oxygen sites of the surface oxygen of pseudobrookite by single hydrogen bonding. This type of bonding enables mobility of water molecules. Further increase in humidity results in increase of the multilayer physical adsorption. The physisorbed water molecules are ionized and produce a large number of hydronium ions as charge carriers. This results in the formation of a liquid-like network. In very high humidity conditions the amount of water increases so the physisorbed water layers behave like a normal condensed liquid where protons require low energy for hopping between adjacent water molecules. This results in increase of ionic conductivity. The Grotthuss charge mechanism can be used to explain conductivity [24]:

$$H2O + H3O^+ \rightarrow H3O^+ + H2O, \quad (4)$$

where charge transport occurs when H_3O^+ releases a pro- ton to a nearby H_2O molecule. It is ionized and forms another H_3O^+, resulting in hopping of protons from one water molecule to another. Electrolytic conduction occurs in the liquid layer in addition to protonic conduction in the adsorbed layers, further enhancing conductivity. The inter- action between water and the sample porous structure also needs to be taken into account as open pores enable water condensation in the capillary pores. This directly depends on the sample microstructure,

namely the available pore sizes and their distribution.

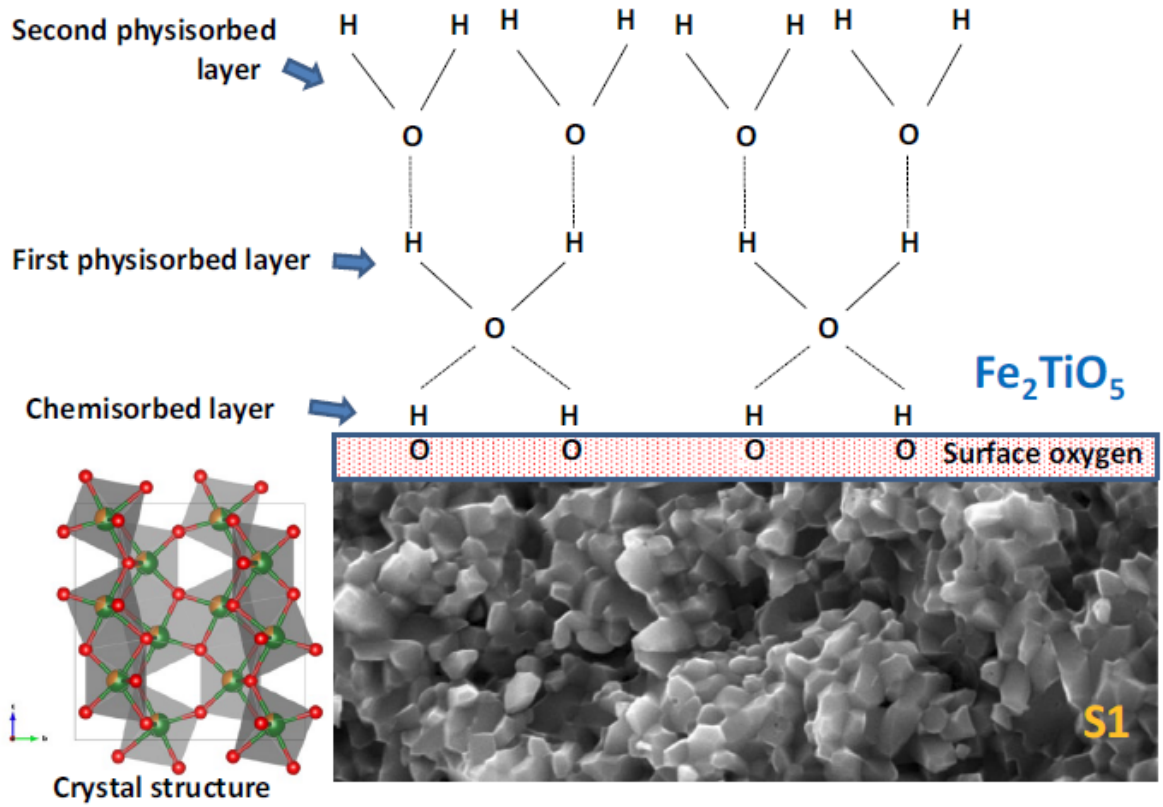

Fig. 7 Schematic illustration of the humidity sensing mecha- nism (microstructure of sample 1), pseudobrookite crystal structure drawn using VESTA [25]

In the case of pseudobrookite, impedance and resistance are reduced by proton hopping, electronic and ionic diffusion, transport and polarization mechanisms with increase in humidity [26]. Differentiation of the processes occur- ring with increase in humidity is possible from analysis of the slope of the change in impedance and sensitivity. In the case of sample S2, its inhomogenous microstructure with large rod grains of pseudobrookite surrounded with smaller pseudobrookite and some rutile grains (Fig. 2c, f) exhibits the lowest response to change in humidity at all three analyzed temperatures. Sample S1 (Fig. 2a, b) with the smallest grain size and density improves with increase in operating temperature. In this case we can also clearly differentiate the change in the impedance slope with increase in humidity at different temperatures (Fig. 5, at 70% RH at 20 °C, moving to lower humidity values with increase in temperature), indicating a change in the humid- ity sensing mechanism. Sample S3, that has a relatively high density and uniform

microstructure (Fig. 2e, d) shows the highest sensitivity to humidity at 20 °C (Fig. 6), but with increase in operating temperature the sensitivity of S1 improves, resulting in values similar to S3.

3.5 Dielectric constant and loss tangent

As expected and in accordance with previous analysis of pseudobrookite bulk samples [19] the dielectric constant (real component of dielectric permittivity) values of samples S1, S2 and S3 decreased continually with increase in frequency and increased with increase in sample temperature. This reflects the usual dielectric dispersion and can be attributed to polarization due to changes in valence states of cations and space charge polarization. With increase in humidity the dielectric constant also increases. An example of the change of the dielectric constant with frequency for different humidity values at the operating temperature of 40 °C is shown in Fig. 8a, with the inset showing how the dielectric constant changed for two characteristic humidity values (40 and 90%) at all three analyzed operating temperatures. The highest values were obtained for sample S3 at the operating temperature of 60 °C and humidity of 90%. In all cases there is a significant difference at low frequencies in the dielectric constant values obtained for RH 40 and 90%, reflecting the influence of humidity. According to Ahmad et al. [27], the large degree of dispersion present for high RH can be attributed to the charge transfer within the interfacial diffusion layer present between the electrodes and the adsorbed water. Figure 8b shows how the dielectric constant changed for samples S1, S2 and S3 at 100 Hz with humidity at operating temperatures of 20 and 40 °C, confirming again the change in the dielectric constant for increased RH and influence of the analyzed sample microstructure.

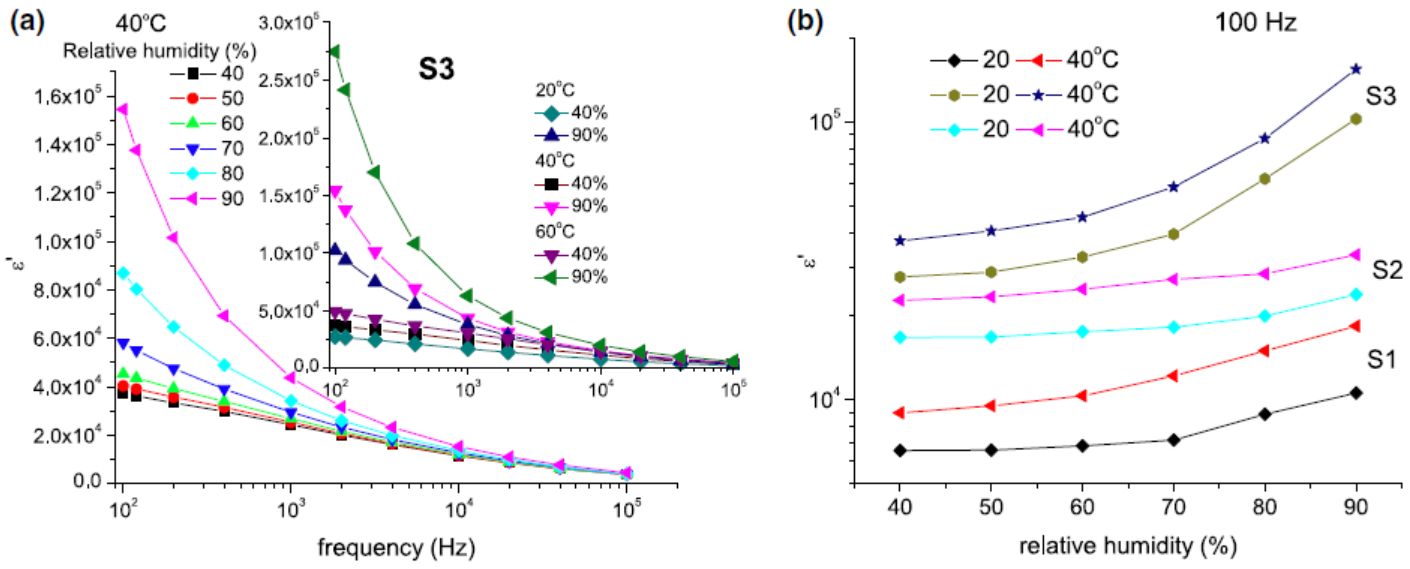

Fig. 8 Change in dielectric constant for **a** sample S3 with frequency for different humidity, **b** samples S1, S2 and S3 with humidity at 20 and 40 °C

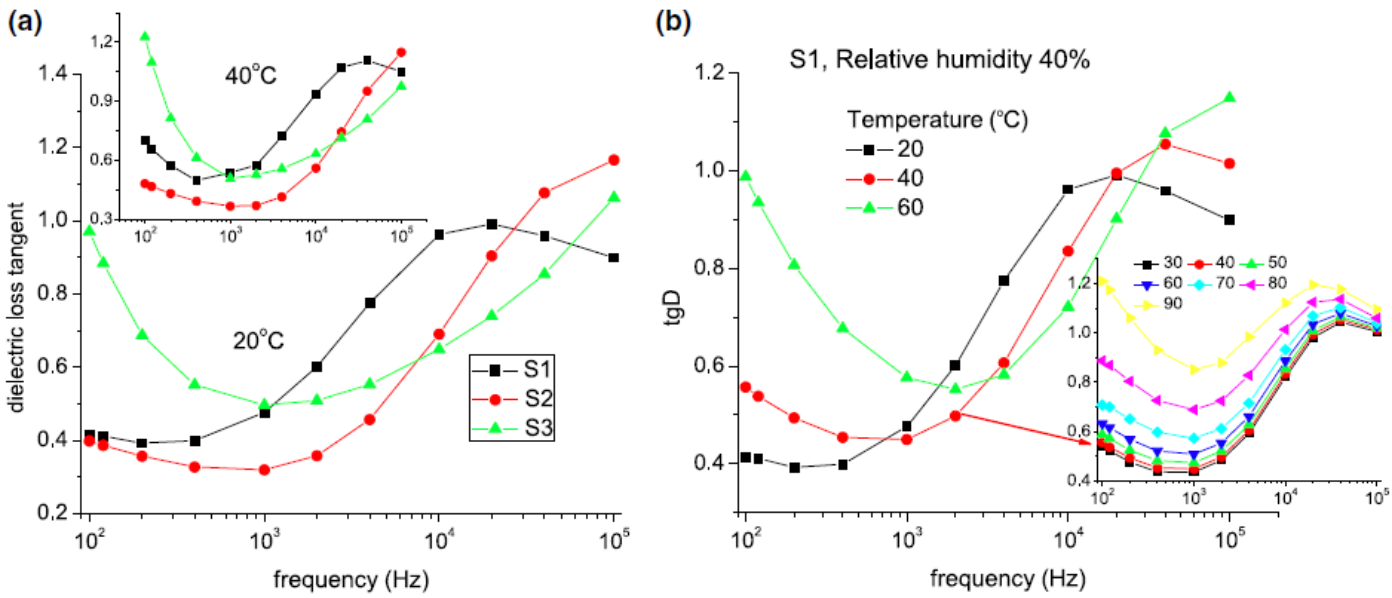

Fig. 9 Change in dielectric loss tangent for **a** samples S1, S2 and S3 at 20 and 40 °C, relative humidity 40%, **b** sample S1 with frequency at 20, 40 and 60 °C relative humidity 40%, inset: at 40 °C for humidity 30–90%

The frequency dependence of the dielectric loss tangent is shown in Fig. 9. Generally, it decreases with increase in frequency, followed by an increase and maximum at higher

frequencies and they vary depending on the analyzed sample (Fig. 9a). The observed maximum corresponds to a dielectric relaxation phenomenon [27]. In the analyzed frequency range, at 20 °C a clear minimum and maximum can be observed for sample S1, a minimum and part of maximum for sample S2, while only a minimum can be observed for sample S3. This shows shifting of the maximum to higher frequencies depending on the sample microstructure (grain size, porosity). Increase in the operating temperature leads to a shift in the minimum and maximum towards higher frequencies as shown in the inset for samples S1, S2 and S3 at 40 °C and sample S1 on Fig. 9b. The influence of humidity is reflected in an overall increase in the dielectric loss tangent at a given operating temperature with a slight shift of the observed minimum and maximum towards higher frequencies as shown in the inset on Fig. 9b.

3.6 Conductivity

The change in conductivity with increase in frequency obeyed a similar dependence for all three investigated samples (S1, S2 and S3) as shown in Fig. 10. Conductivity increased with increase in sample temperature and increase in humidity. If we compare the values obtained for different samples, the lowest values were obtained for sample S1 at 20 °C, with conductivity increasing with sample temperature (40 and 60 °C) for the same humidity. Overall sample S2 had a higher conductivity than S1 at the same temperature, and S3 the highest, as shown in Fig. 9a, b. This shows a clear dependence on sample density and microstructure. In all cases the conductivity followed the hopping dynamics of charge carriers in accordance with the Jonscher power law [26, 28]:

$$\sigma_{AC} = \sigma_{DC} + A\omega^{s} \qquad (5)$$

where σ_{DC} is the DC conductivity, A is the pre-exponential factor and s is the frequency exponent (between 0 and 1). The values obtained for the frequency exponent varied between 0.4 and 0.87 and insets in Fig. 10a, b show that this parameter decreased with increase in sample temperature and humidity. For sample S2 these changes were the small- est and ranged between 0.88 and 0.73 for all three analyzed temperatures and the humidity range 30–90%, as shown in Fig. 10a for S2 at 20 °C. In the case of S1 the change was more expressed at 60 °C compared to 20 °C.

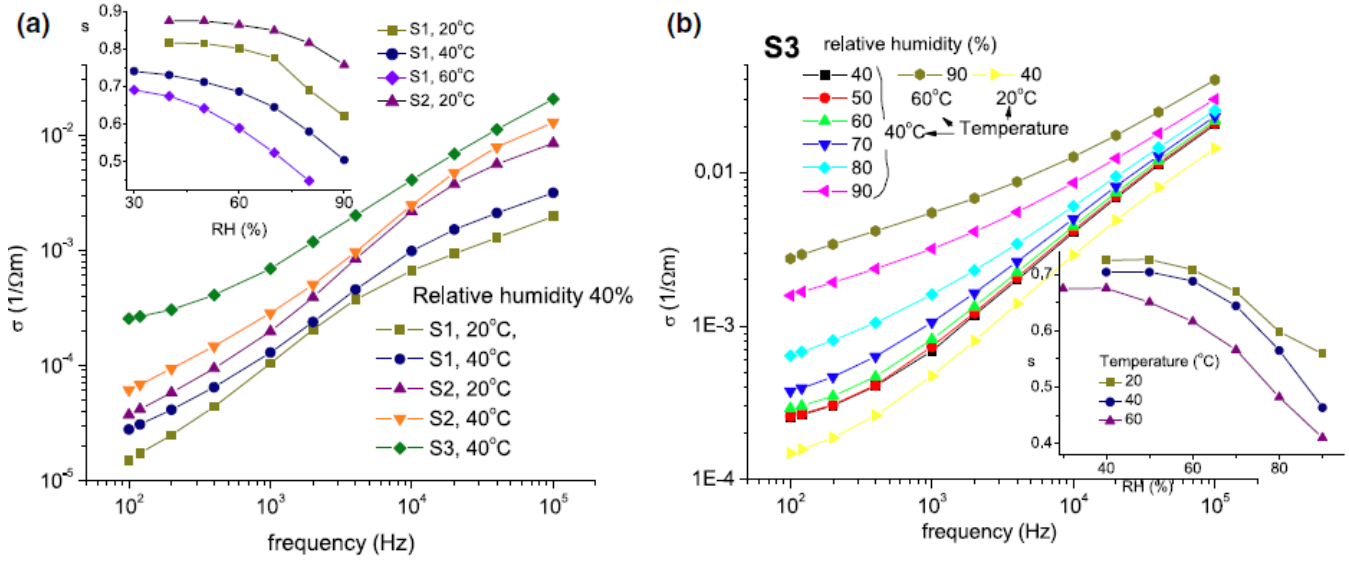

Fig. 10 Frequency dependence of electrical conductivity for **a** relative humidity 40% samples S1, S2, 20 °C and S1, S2, S3, 40 °C, inset variation of frequency exponent *s* for S1 and S2 with humidity and temperature **b** sample S3 at 20 °C, relative humidity (RH) 40%, 40 °C RH 40–90% and 60 °C RH 90%, inset variation of frequency exponent *s* with sample humidity and temperature

Our previous analysis of electrical conductivity of pseudobrookite [26] showed that the frequency exponent increased both for bulk samples and powder compacts with increase in sample temperature above room temperature (300–423 K). In this case the conduction mechanism could be described as small polaron hopping. The increase in temperature was also reflected in the change of the shape of the electrical conductivity curve with more of the curve representing the DC component of conductivity that is independent of frequency. In the temperature range below room temperature (150–300 K). Sharma et al. [29] deter- mined that the conduction mechanism occurred through polaron hopping following the correlated barrier hopping model. We have analyzed the change in conductivity at three temperatures in different humidity conditions (RH 30–90%). For all three samples the frequency exponent decreased with increase in sample temperature for the same RH levels. This shows the conduction mechanism can be described as polaron hopping following the correlated barrier hopping model [30–32]. Change in conduction with increase in humidity in ceramic porous materials is due to the humidity sensing mechanism described in detail above. This process is a surface mechanism [33]. At lower humidity values, during the chemisorptions process of water molecules the concentration of mobile ions is independent of RH [27]. As the humidity increases and physisorption starts conductivity increases. Ahmad et al. [27], ascribed the

increase in conductivity to a percolation-type conduction mechanism within the physisorbed layer. At high humidity levels, in our case RH 70–90% proton hopping between nearest neighbor water molecules requires low energy and is intensified and this is reflected in the change of the frequency exponent with increase in humidity. In our case this is all influenced by the sample microstructure, with much more expressed changes obtained for samples S3 and S1, compared to sample S2. According to Chou et al. [34] at low humidity surface area and water adsorption have a dominant influence, while for high humidity the mesopore volume and capillary condensation becomes an important factor.

3.7 Complex impedance analysis

Complex impedance plots obtained for samples S1, S2 and S3 gave similar curves in the shape of part of a depressed semicircular arc reflecting the dominant influence of the grain boundary component [19, 26]. Higher values were obtained for S1 than S2 and the lowest for S3 reflecting the influence of sample microstructure and density (due to different sintering temperatures). Complex impedance values for all three analyzed samples decreased (and show- ing more of the semicircle) with increase in sample temperature, as shown in Fig. 11a for sample S1. Increase in humidity reduced the complex impedance. Shrinking of the complex impedance semicircle (or its part) with increasing humidity can be attributed to hopping of H^+ via H_2O in physisorbed water [10]. An example is given in Fig. 11b for sample S3 at 40 °C, showing the change in complex impedance in the humidity range 40–90%. Complex impedance diagrams are similar for lower RH of 40 and 50%, and shrank with increase in humidity. This is in correlation with the described humidity sensing mechanism and change in impedance and dielectric constant with humidity shown in Figs. 5 and 8.

At 20 °C (samples S1 and S2) in the relative humid- ity range 40–90% besides the dominant influence of the grain boundary component, a small part of a semicircle at higher frequencies (around 20 kHz, as shown in Fig. 11a) reflected the influence of the grain component. This remained noticeable for sample S1 at 40 °C, while only one semicircle was noted at 60 °C. In the case of sample S2, the grain component could be noted only at 20 °C. In the case of sample S3 (Fig. 11b) at all analyzed temperatures only one semicircle was noted for the analyzed relative humidity range reflecting the dominant influence of one relaxation mechanism.

Impedance data were analyzed using an equivalent circuit consisting of a resistance denoting the grain component connected with a parallel resistance and constant phase

(CPE) element denoting the grain boundary component (Fig. 11b). The CPE element was used to replace the capacitor as previously described in detail in [19, 26]. Analysis and simulation of impedance spectra was per- formed using the EIS Spectrum Analyzer software [35] yielding a good fit with an average error of about 2%, as shown in the inset on Fig. 11b confirming the dominant influence of grain boundaries.

3.8 Hysteresis

Absorption/desorption RH hysteresis curves obtained for samples S1, S2 and S3 are shown in Fig. 12. Hysteresis measurements were performed at 25 °C (room temperature) at the frequency of 100 Hz, RH ranging from 40 to 90%. Hysteresis represents the time lag in the absorption (condensation) and desorption (evaporation) process and it can be due to disordered mesoporous solids [10]. In our case the highest value was obtained for sample S2 of 6.15%, while samples S1 and S3 had lower values of 3.6 and 2.99%. The difference can be ascribed to the differences in microstructure, where sample S2 had an inhomogenous microstructure compared to samples S1 and S3.

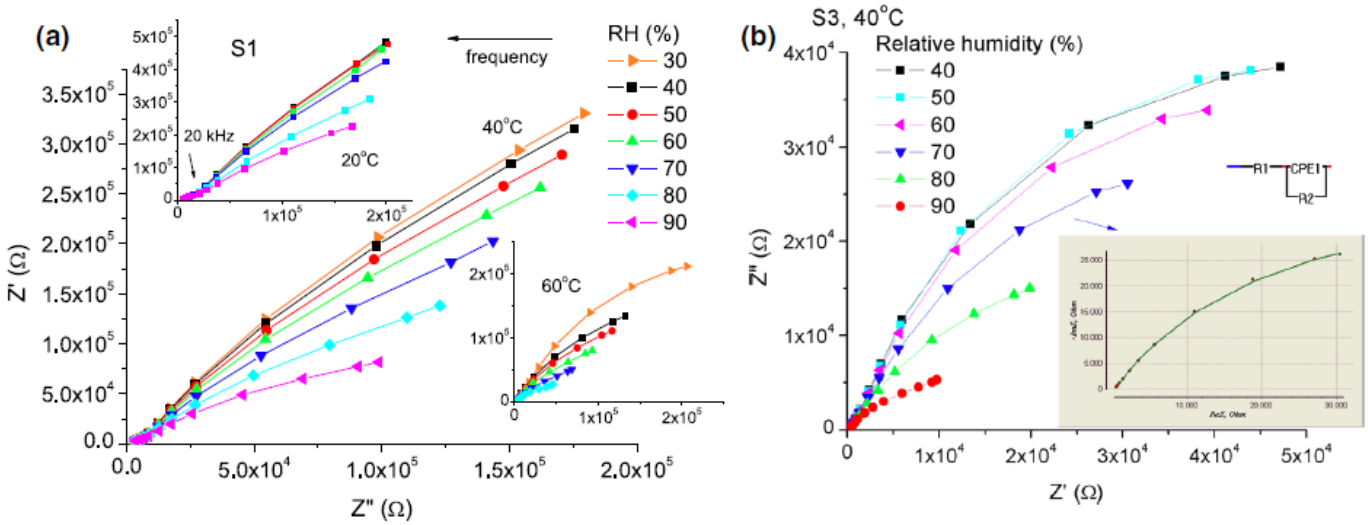

Fig. 11 Complex impedance diagrams for **a** sample S1 at 20, 40 and 60 °C and humidity 30–90%, **b** sample S3 at 40 °C, humidity 40–90%, inset example of fitted curve at humidity 80% using the shown equivalent circuit

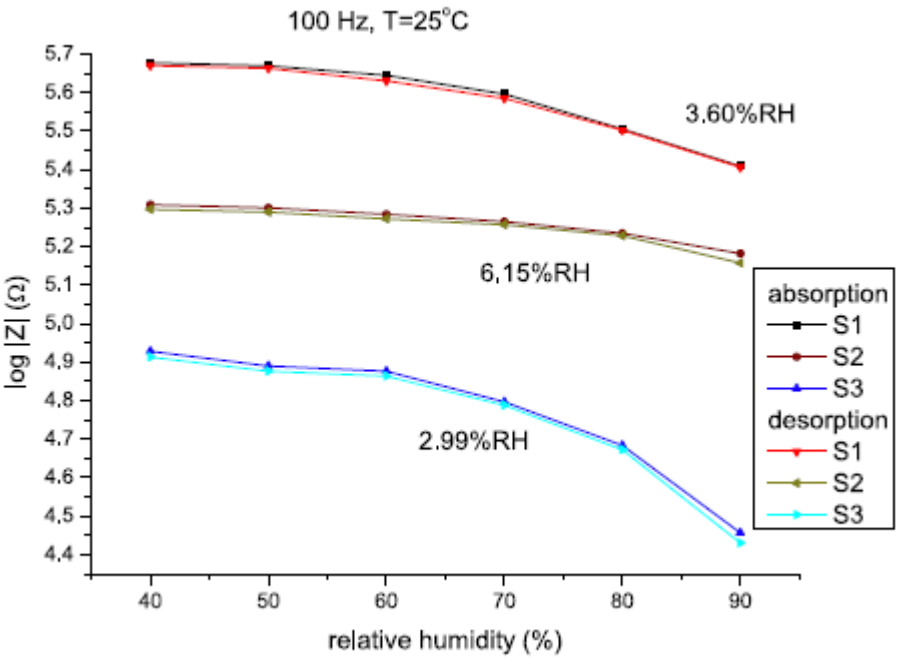

Fig. 12 Absorption and desorption (hysteresis) curves for samples S1, S2 and S3 at 100 Hz and 25 °C

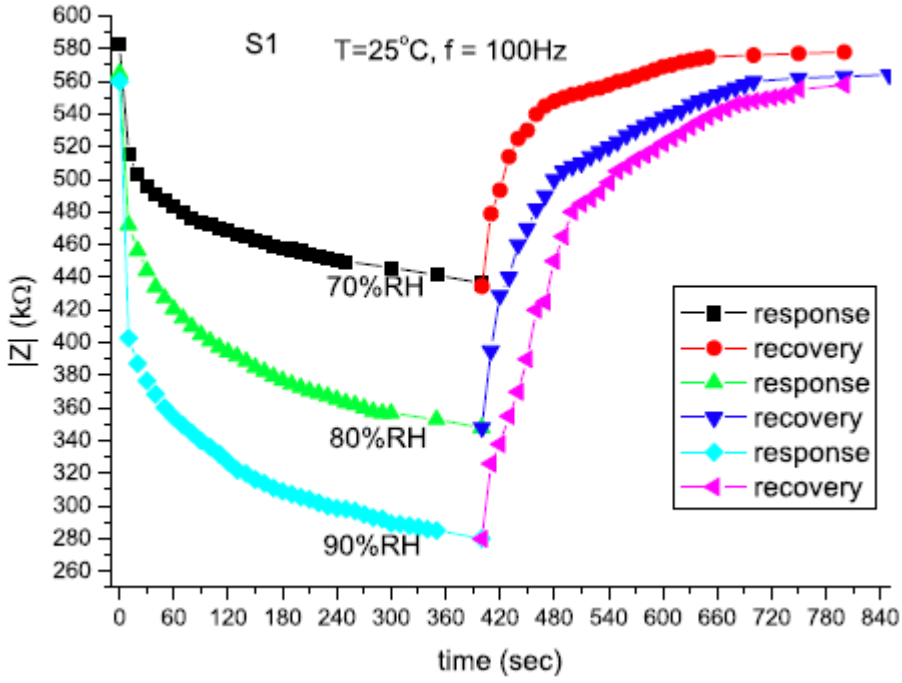

Fig. 13 Response and recovery curves of sample S1 for relative humidity of 70–90%

3.9 Response and recovery time

The response and recovery times are important in evaluating the efficiency of humidity sensors [14]. The response time of a sensor can be defined as the time needed for the sensor to reach 90% of the total impedance/resistance/change when exposed to relative humidity created in the chamber, while the recovery time of a sensor can be defined as the time required for the resistance/impedance to return to 90% of the original baseline signal [3, 9, 13, 14]. The response and recovery characteristics of samples S1 and S3 were measured at 100 Hz at room temperature of 25 °C, for three relative humidity (RH) levels 70, 80 and 90%. Samples were inserted into the chamber which had previously reached equilibrium for the set humidity. Figure 13 shows the aver- age values that were obtained for 90% RH. Both samples S1 and S3 responded in a similar way for all three investigated humidity levels and the average time for response to was 206 s for S1 and 170 s for S3, while average recovery values were 210 s for S1 and 140 s for S3. These values are not low, actually quite high for any practical applications. They are compatible for some literature values also obtained for bulk samples [10, 36–38]. Further research will focus on pseudobrookite thick films, where shorter response and recovery times are expected.

4 Conclusion

Pseudobrookite bulk samples were obtained by sintering hematite and anatase nanopowders (60:40 wt% ratio) at 950, 1050 and 1150 °C. The change in relative humidity at all three analyzed operating temperatures (20, 40 and 60 °C) had a noticeable influence on measured impedance, resistance and capacitance that was correlated with obtained microstructures confirming the potential of pseudobrookite as a possible humidity sensing material. A detailed analysis of dielectric properties (dielectric constant, loss tangent) reflected the influence of relative humidity and could be explained by the humidity sensing mechanism of chemisorption and physisorption and the Grotthuss charge mechanism. Electrical conductivity increased with increase in sample temperature and with increase in relative humid- ity. It followed the Jonsher power law and the change in the frequency constant showed that in conditions of relative humidity between 40 and 90% the conduction mechanism can be explained by the correlated barrier hopping model. Analysis of complex impedance showed that with increase in humidity the semicircle arc decreased and its shrinking for high relative humidity can be attributed to hopping of H^+ via H_2O in physisorbed water. Complex

impedance was modeled using an equivalent circuit that confirmed the dominant influence of the grain boundary component.

Acknowledgements This work was performed as part of Project III45007 financed by the Ministry for Education, Science and Techno- logical Development of the Republic of Serbia.

References

1. T.A. Blank, L.P. Eksperiandova, K.N. Belikov, Sens. Actuators B **228**, 416 (2016)
2. H. Faharani, W. Wagiran, M.N. Hamida, Sensors **14**, 7881 (2014)
3. A. Mirzaei, B. Hashemi, K. Janghorban, J. Mater. Sci.: Mater. Electron. **27**, 3109 (2016)
4. A. Sutka, K.A. Gross, Sens. Actuators B **222**, 95 (2016)
5. V. Jeseenthrani, M. George, B. Jeyaraj, A. Dayalan, K.S. Nagaraja, J. Exp. Nanosci. **8**, 358 (2013)
6. K. Arshaka, K. Twomey, D. Egan, Sensors **2**, 50 (2002) A. Cavalieri, T. Caronna, I. Natali Sorra, J.M. Tulliani, Ceram. Int. **38**, 2865 (2012)
7. A.E. Mahmoud, G. Viola, A.S. Afify, A.M. Babeer, M. Ferraris, J. Porous. Mater. https://doi.org/10.1007/s10934-016-0315-8
8. A. Tripathy, S. Pramqanik, A. Manna, S. Bhuyan, N.F.A. Shah,
9. Z. Radzi, N.A.A. Osman, Sensors **16**, 1135 (2016)
10. J. Shah, R.K. Kotnala, B. Singh, H. Kishnan, Sens. Actuators B **128**, 306 (2007)
11. M.R. Mohammadi, D.J. Fray, Physica E **46**, 43 (2012)
12. P.M. Faia, J. Libardi, Sens. Actuators B **236**, 682 (2016)
13. M. Sabarilakshmi, K. Janaki, J. Mater. Sci.: Mater. Electron. **28**, 8101 (2017)
14. P. Rao, R.C. Chikate, S. Bhagwat, New J. Chem. **40**, 1720 (2016)
15. J.M. Tulliani, C. Baroni, L. Zavattaro, C. Grignani, Sensors **13**, 12070 (2013)
16. J.M. Tulliani, P. Bonville, Ceram. Int. **31**, 507 (2005)
17. G. Neri, A. Bonavita, S. Galvagno, N. Donato, A. Caddemi, Sens. Actuators B **111–112**, 71 (2005)
18. Q. Liu, J. He, T. Yao, Z. Sun, W. Cheng, S. He, Y. Xie, Y. Peng, H. Cheng, Y. Sun, Y. Jiang, F. Hu, Z. Xie, W. Yan, Z. Pan, Z. Wu, S. Wei, Nat. Commun. **5**, 5122 (2014)
19. Z.Z. Djuric, O.S. Aleksic, M.V. Nikolic, N. Labus, M. Rado- vanovic, M.D. Lukovic, Ceram. Int. **40**, 15131 (2014)
20. R. Yu, Z. Li, D. Wang, X. Lai, C. Xing, M. Yang, X. Xing, Scripta Mater. **63**, 155 (2010)
21. G. Miskovic, M.D. Lukovic, M.V. Nikolic, Z.Z. Vasiljevic, J. Nicolics, O.S. Aleksic,

Analysis of electronic properties of pseudobrookite thick films with possible application for NO gas sensing, Proceedings of the 39th International Spring Seminar on Electronics Technology (ISSE), 18–22 May, 2016, https://doi. org/10.1109/ISSE.2016.7563226

22. S.N. Patil, A.M. Pawar, S.K. Tilekar, B.P. Ladgaonkar, Sens. Actuators A **244**, 35 (2016)

23. M. Egashira, M. Nakashima, S. Kawasumi, T. Selyama, J. Phys. Chem. **85**, 4125 (1981)

24. N. Agmon, Chem. Phys. Lett. **244**, 456 (1995)

25. K. Momma, F. Izumi, J. Appl. Crystallogr. **44**, 1271 (2011)

26. M.V. Nikolic, D.L. Sekulic, Z.Z. Vasiljevic, M.D. Lukovic, V.B. Pavlovic, O.S. Aleksic, J. Mater. Sci.: Mater. Electron. **28**, 4796 (2017)

27. M.M. Ahmad, S.A. Makhlouf, K.M.S. Khalil, J. Appl. Phys. **100**, 094323 (2006)

28. A.K. Jonscher, Nature **267**, 673 (1977)

29. S. Sharma, T. Basu, A. Shahee, K. Singh, N.P. Lalla, J. Alloys Compd. **663**, 289 (2016)

30. H. Agarwal, T.P. Yadav, O.N. Srivastava, M.A. Shaz, Ceram. Int. **43**, 16986 (2017)

31. M.M. El-Nahass, A.A. Attia, G.F. Salem, H.A.M. Ali, M.I. Ispail, Physica B **434**, 89 (2014)

32. E.V. Gopalan, K.A. Mallini, S. Sagar, D.S. Kumar, Y. Yoshida, I.A. Al-Omari, M.R. Anantharaman, J. Phys. D **42**, 165005 (2009)

33. G. Garcia-Belmonde, V. Kytin, T. Dittrich, J. Bisquert, J. Appl. Phys. **94**, 5261 (2003)

34. K.-S. Chou, T.-K. Lee, F.-J. Liu, Sens. Actuators B **56**, 106 (1999)

35. A.S. Bondarenko, G. Ragoisha, EIS Spectrum Analyzer, http:// www.abc.chemistry.bsu.by

36. Sutka, G. Mezinkis, A. Lusis, D. Jakovlevs, Sens. Actuators B **171–172**, 204 (2012)

37. R.B. Kamble, V.I. Mathe, Sens. Actuators B **131**, 205 (2008)

38. M. Li, X.I. Chen, D.F. Zhang, W.Y. Wang, W.J. Wang, Sens. Actuators B **147**, 447 (2010)